AIP Advances

Phase changeable vanadium dioxide (VO_2) thin films grown from vanadium pentoxide (V_2O_5) using femtosecond pulsed laser deposition

Cite as: AIP Advances **10**, 065225 (2020); https://doi.org/10.1063/5.0010157
Submitted: 07 April 2020 . Accepted: 31 May 2020 . Published Online: 17 June 2020

Eric Kumi-Barimah, Dimitris E. Anagnostou, and Gin Jose

COLLECTIONS

Paper published as part of the special topic on Chemical Physics, Energy, Fluids and Plasmas, Materials Science and Mathematical Physics

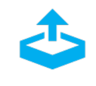

ARTICLES YOU MAY BE INTERESTED IN

Grain size effect on the semiconductor-metal phase transition characteristics of magnetron-sputtered VO_2 thin films
Applied Physics Letters **87**, 051910 (2005); https://doi.org/10.1063/1.2001139

Potential low powered smart window coating using a stoichiometrically downgraded vanadium oxide thin film structure
AIP Advances **10**, 065201 (2020); https://doi.org/10.1063/1.5145019

Plasma-enhanced pulsed laser deposition of copper oxide and zinc oxide thin films
AIP Advances **10**, 065323 (2020); https://doi.org/10.1063/5.0008938

© 2020 Author(s).

Phase changeable vanadium dioxide (VO_2) thin films grown from vanadium pentoxide (V_2O_5) using femtosecond pulsed laser deposition

Cite as: AIP Advances 10, 065225 (2020); doi: 10.1063/5.0010157
Submitted: 7 April 2020 • Accepted: 31 May 2020 •
Published Online: 17 June 2020

View Online

Export Citation
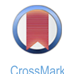
CrossMark

Eric Kumi-Barimah,[1,a)] Dimitris E. Anagnostou,[2] and Gin Jose[1]

AFFILIATIONS

[1] School of Chemical and Process Engineering, University of Leeds, Clarendon Road, Leeds LS2 9JT, United Kingdom
[2] Engineering and Physical Sciences, Heriot-Watt University, Edinburgh EH14 4AS, United Kingdom

[a)] Author to whom correspondence should be addressed: e.kumi-barimah@leeds.ac.uk

ABSTRACT

There are significant challenges accompanied by fabricating a pure crystalline VO_2 (M1) thin film with an abrupt metal to insulator phase change properties. Most fabrication methods yield an amorphous VO_2 thin film that requires a post-annealing process to be converted into crystalline VO_2 (M1). Hence, the thickness of VO_2 (M1) films produced is very limited. In this work, we report the growth of pure VO_2 (M1) crystalline thin films onto a sapphire substrate in an oxygen atmosphere by the femtosecond pulsed laser deposition technique and using vanadium pentoxide (V_2O_5) as an ablation target. The thin films were deposited at substrate temperatures of 25 °C, 400 °C, and 600 °C, which reveal the crystallized structures of VO_2 (M1) without post-annealing. The thin film deposited at a substrate temperature of 600 °C exhibits a sharp and an abrupt metal-to-insulator transition (MIT) at a temperature of 66.0 ± 2.5 °C with nearly four orders of magnitude of the resistivity change (3.5 decades) and a narrow MIT hysteresis width of 3.9 °C. Furthermore, the influence of the substrate temperature, nanoparticle or grain size, and film thickness on the MIT parameters such as sharpness of the transition temperature, hysteresis width, and amplitude are discussed for potential applications of tunable antennas, terahertz planar antennas, and RF-microwave switches.

© 2020 Author(s). All article content, except where otherwise noted, is licensed under a Creative Commons Attribution (CC BY) license (http://creativecommons.org/licenses/by/4.0/). https://doi.org/10.1063/5.0010157

I. INTRODUCTION

Vanadium is a well known ductile metal with a strong attraction for oxygen, which leads to the formation of multiphase states such as VO_2, V_2O_3, V_2O_5 V_3O_5, $V_{14}O_6$, V_6O_{13}, etc.[1–5] Moreover, there are many polymorphic structures of vanadium dioxide (VO_2), including M1, M2, A, B, C, and R with the same chemical formula[6,7] and completely different crystalline structures. This clearly demonstrates the complexity of the vanadium–oxygen polymorph crystallographic structure. Among these, vanadium-dioxide VO_2 (M1) polymorph phase thin films have received a great deal of attention in the recent years due to their remarkable physical, chemical, optical, and electrical properties. VO_2 (M1) undergoes reversible semiconductor metal-to-insulator transition (MIT) in rutile-type, which starts from the room temperature insulating state to the metallic state at a temperature around 68 °C.[8] This phase transition is accompanied by a structural change from a lower temperature monoclinic crystal to a higher temperature tetragonal rutile polymorph phase subsequently exhibiting the electrical resistivity change from three to five orders of magnitude. The fast switching of the VO_2 crystalline phase can be stimulated by external stimuli such as electrical, optical, and thermal activation,[9–14] thus leading to change in the thermal, electrical, magnetic, and optical properties. The change in the phase by external stimuli is reversible through the normal cooling process. These outstanding properties of the VO_2 (M1) thin film are attractive for designing ultrafast optical switches, thermochromic smart windows, modulation of near-infrared wavelengths, RF-microwave switches, THz metamaterial devices, phase shifters, power limiters, tunable and reconfigurable antennas and microwave devices, nano-resonators, and smart radiation devices for spacecraft applications.[15–25]

© Author(s) 2020

There are significant challenges and difficulties accompanying the synthesis of a pure VO_2 (M1) thin film, which could exhibit sharp MIT with a narrow hysteresis width. The MIT properties depend on multiple factors, including fabrication techniques, crystallinity or grain size, deposition or post-annealing temperature, doping impurity, stoichiometry, oxygen deficiency, and strain.[26–30] Despite this, the vanadium ions and oxygen stoichiometry ratio have a considerable influence on the vanadium oxide system formation, electrical, and optical properties. As a consequence, several fabrication techniques such as sputtering,[31] molecular beam epitaxy,[32] atomic layer deposition,[33] and nanosecond pulsed laser deposition (PLD)[8,34,35] have been employed to the deposition of various vanadium–oxygen polymorphic phases. Among these fabrication techniques, PLD has shown to be highly efficient for stoichiometry mass transfer from the target material to the substrate surface along with high deposition rates. Conversely, most of the VO_2 thin films synthesized by the PLD method have employed KrF excimer and Nd:YAG nanosecond (ns) lasers.[36–39] The ns-PLD ablation of a target material creates a continuous heat-affected zone on the surface of the material with a laser-induced shock. This leads to the formation of broader and cluster microparticles due to the subsurface superheating of the target material during evaporation or ablation owing to the long pulse duration of the ns-laser.[40] Furthermore, recent studies suggest that most vanadium oxide (V_xO_y) thin films fabricated by ns-PLD require post-deposition annealing in various gas atmospheres such as oxygen or mixture of oxygen and nitrogen so as to form VO_2 (M1) stoichiometry.[41–43] On the other hand, femtosecond (fs)-PLD ablation is significantly different from ns-PLD and is an effective method of producing nanoparticles without introducing any thermal heating effect onto the target surface. This is attributed to the time scale of the fs-laser matter interaction of the target material, which is presided by the ultrashort pulse duration. The plasma plume created by fs-laser interaction with a target consists of the nanoparticles of sizes ranging from 10 nm to 100 nm[44] through the optimization of the laser fluence, which accumulate to form a thin film on a substrate with a minimal surface roughness and change in stoichiometry. The fs-laser interaction with various target materials and nanoparticles generation has already been discussed extensively elsewhere.[18,45] Hence, it is worth investigating the fs-PLD fabrication of the VO_2 thin film to better understand the relationship between nanoparticles or grain sizes, film thickness, and a structural phase transition on the MIT parameters.

Here, we present the high rate synthesis of thick and good quality polycrystalline VO_2 thin films on the sapphire substrate by using a less expensive vanadium pentoxide (V_2O_5) target and the fs-PLD technique. We carried out the single step process of fabricating a pure VO_2 thin film by ablating the V_2O_5 target under the oxygen atmosphere via fs-PLD. The influence of the substrate temperature on the grain sizes, VO_2 thin film thickness, crystalline structure evaluation, the change in electrical resistivity from insulating to metallic phase, transition temperature, and hysteresis width of the films grown is discussed in this paper.

II. EXPERIMENTAL DETAIL

A commercially available V_2O_5 powder (high purity grade 99.95%) was obtained from Alfa Aesar, and then pressed into a tablet with a dimension of $30 \times 30 \times 3.5$ mm^3 and was used as an ablation target for fs-PLD. A KMLabs Wyvern™ 1000-10 amplifier solid-state Ti:sapphire laser (central wavelength of 800 nm, repetition rate of 10 kHz, full width half maximum (FWHM) of 60 nm, pulse duration of ~40 fs) was used to ablate the V_2O_5 target onto the sapphire (0001) substrate, which was converted into a VO_2 thin film upon careful optimization of the deposition parameters. The sapphire substrates of 650 μm thick were initially cleaned with deionized water at a temperature of 50 °C, followed by cleaning with acetone and isopropanol for 15 min, and finally dried with a clean lens tissue. The target-to-substrate distance was maintained at 70 mm during the deposition. V_2O_5 nanoparticles were initially deposited on the sapphire substrate for 12 min at room temperature with the laser fluence range from 0.16 J/cm^2 to 0.49 J/cm^2 to establish the ablation threshold of the target material. This was found to be 0.27 J/cm^2. Prior to VO_2 thin film fabrication, a customized PLD chamber (PVD Products) was pumped down to a base pressure of 10^{-6} Torr, and then injected with a high purity oxygen as a background gas maintaining the chamber pressure at ~70 mTorr. The substrate temperatures during the film growth were held at 25 °C (SP25), 400 °C (SP400), and 600 °C (SP600), while a laser fluence of 0.27 J/cm^2 was used to ablate the target. The thin films were deposited onto the sapphire substrates over a time period of 120 min.

The surface morphology and microstructure of the films were initially characterized by scanning electron microscopy (SEM), while the size distribution of the particles was processed by using the Fiji enhanced ImageJ software. The crystalline phase of the thin films was investigated by x-ray diffraction (XRD) (Philips X'pert MPD instrument) and Raman spectroscopy. A glancing incident angle of 1.0° was employed to measure the XRD patterns of the films using a Philips PANalytical X'pert Diffractometer with Cu Kα radiation (λ = 1.540 56 Å). A Renishaw inVia Raman microscope under an Ar^+ laser (514 nm) excitation was used to measure the vibrational spectra of the V_2O_5 target and as-deposited thin films, whereas, the cross section and the thin film thicknesses were examined with a focused ion beam (FIB, FEI Helios G4 CX DualBeam). The electrical resistivity switching of the thin films was also examined with a two-point probe made contacts technique at a temperature range from 20 °C to 100 °C.

III. RESULTS AND DISCUSSION

A. Surface morphology and crystalline structure evaluation

Knowing that the fs-PLD thin film is formed by the accumulation of nanoparticles, V_2O_5 nanoparticles were initially deposited on the sapphire substrate at room temperature for 12 min by varying the laser fluence and keeping the other deposition parameters the same as that of samples SP25, SP400, and SP600. Figure 1 illustrates the SEM images of the particles deposited by using different laser fluences of 0.16 J/cm^2, 0.27 J/cm^2, and 0.49 J/cm^2. The particles are well dispersed across the entire substrate, as shown in Figs. 1(a) and 1(b), while Fig. 1(c) exhibits agglomerated particles. It is evident that an increase in the laser fluence leads to increase in the particle size and deposition rate. The ImageJ software was used to estimate the average diameter of V_2O_5 nanoparticles or their grain size. The SEM images have a resolution of 1280 × 980 pixels, horizontal and vertical

© Author(s) 2020

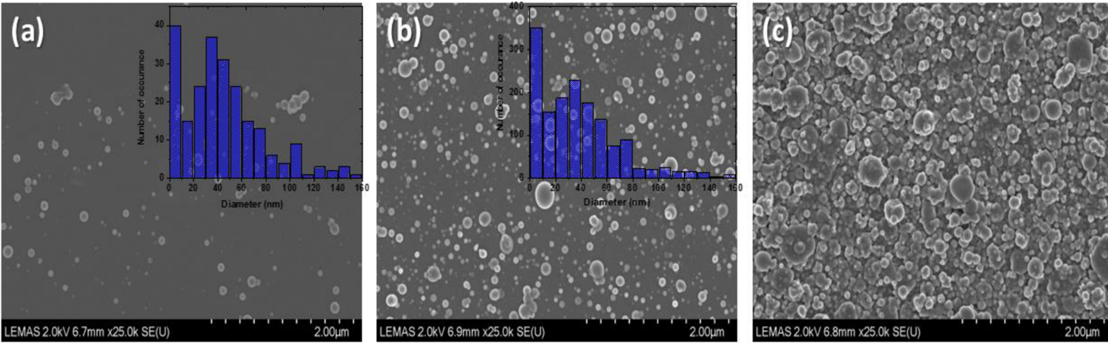

FIG. 1. SEM images of V_2O_5 nanoparticles deposited on the sapphire substrate at room temperature and 70 mTorr oxygen background gas while varying the laser fluences: (a) 0.16 J/cm^2, (b) 0.27 J/cm^2, and (c) 0.49 J/cm^2.

widths of 5.07 × 3.80 μm^2 with a pixel corresponding to ∼4 nm. The size distribution of the nanoparticle is shown in the inset in Figs. 1(a) and 1(b). An average diameter of the nanoparticle or grain size is estimated to be 34 ± 2 nm with a maximum particle size less than 160 nm.

The bulk structural properties of the thin films prepared can be quickly assessed by Raman spectroscopy. Figure 2 shows Raman spectra confirming the vibrational modes of the atomic arrangement and the crystal phase of the as-deposited thin films and compared them with the spectrum of the V_2O_5 target. The Raman spectrum of the V_2O_5 target reveals nine Raman-active vibrational modes, which are centered at ∼143 (B_{3g}) cm^{-1}, 196 (A_g) cm^{-1}, 283 (B_{2g}) cm^{-1}, 302 (A_g) cm^{-1}, 404 (A_g) cm^{-1}, 479 (A_g) cm^{-1}, 525 (A_g) cm^{-1}, 699 (B_{2g}) cm^{-1}, and 994 (A_g) cm^{-1}. These vibrational bands relate to the V_2O_5 orthorhombic phase and had been previously reported elsewhere.[46–51] Upon depositing the thin films, the V_2O_5 target material undergoes complete phase transformation to the VO_2 (M1) monoclinic phase at the substrate temperatures of 400 °C and 600 °C. As shown in Fig. 2, the Raman spectra for samples SP400 and SP600 measured at room temperature reveal the vibrational bands of VO_2 (M1) with Raman active vibrational modes located at 143 (B_g) cm^{-1}, 193 (A_g) cm^{-1}, 224 (A_g) cm^{-1}, 260 (B_g) cm^{-1}, 307 (B_g) cm^{-1}, 338 (A_g) cm^{-1}, 389 (B_g) cm^{-1}, 440 (B_g) cm^{-1}, 497 (A_g) cm^{-1}, 614 (A_g) cm^{-1}, and 820 (B_g) cm^{-1}.[52] According to Shvets *et al.*,[52] the vibrational peak found at 193 cm^{-1} is associated with the VO_2 stretching motion of V–V dimers, whereas the band located at 338 cm^{-1} is assigned to the tilting motion of V–V dimers. On the other hand, the thin film deposited at 25 °C (SP25) consists of a mixed-phase of V_2O_5, VO_2 (B), and V_6O_{13}. For instance, the vibration band range from 100 cm^{-1} to 500 cm^{-1}, which is centered at 280 cm^{-1} can be attributed to the mixed-phase of V_2O_5 and VO_2 (R).[53] According to Asmis and Sauer,[54] the vibrational bands peaked at 567 cm^{-1} and 740 cm^{-1} are assigned to V_6O_{13} and V_4O_{11} bonds.

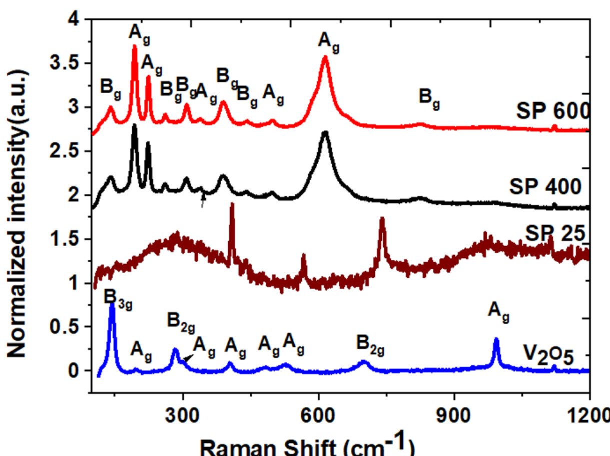

FIG. 2. Raman spectra of the V_2O_5 target and VO_2 thin films fabricated at 25 °C, 400 °C, and 600 °C, respectively.

Besides Raman spectroscopy data, the crystal phase of the V_2O_5 target and as-deposited VO_2 thin films on the sapphire substrate were further confirmed by XRD measurements. A grazing incident angle of 1.0° was employed to measure the XRD diffraction patterns of the target V_2O_5 and films using a Philips PANalytical X'pert Diffractometer with Cu Kα radiation (λ = 1.540 56 Å). Figure 3 illustrates XRD patterns of the V_2O_5 target and VO_2 thin films at the substrate temperatures of 25 °C (SP25), 400 °C (SP400) and 600 °C (SP600) measured within the 2θ range from 5° to 80°, respectively. The XRD patterns of the V_2O_5 target correlate with the standard data available in International Center for diffraction Data (ICDD) card number 00-061-0027 and the orthorhombic phase structure as well as the phase group of P21/m. Furthermore, the XRD spectra of samples SP400 and SP600 have peaks centered at 2θ = ∼27.9°, ∼37.1°, ∼42.2°, ∼56.9°, ∼65°, and ∼73.5°, which correlate with (011), (200), (210), (220), (013), and (231) reflection planes of monoclinic VO_2 (M1), respectively. This evidently demonstrates the formation of the polycrystalline structure that is ascribed to a single-phase monoclinic VO_2 without any other phases of the vanadium oxide diffraction pattern detected. According to ICDD, the observed peaks in the XRD pattern for SP400 and SP600 can be assigned to a pure monoclinic (M1) crystal structure and phase group of P21/c (ICDD: 00-009-0142). Furthermore, these diffraction patterns are in good agreement with theVO_2 (M1) thin film reported by Brassard *et al.*,[55]

© Author(s) 2020

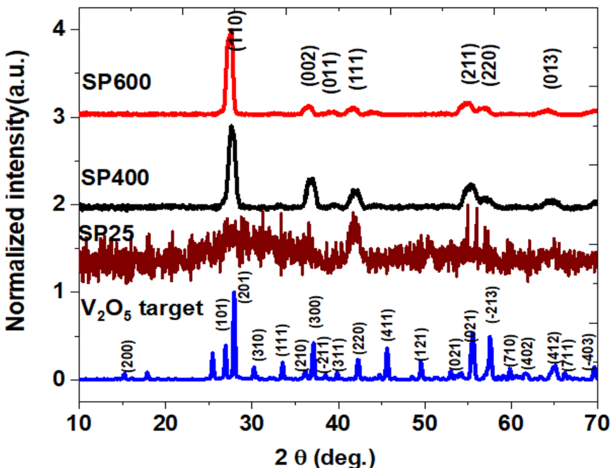

FIG. 3. Grazing-incidence XRD diffraction patterns spectra of the V_2O_5 target and VO_2 thin films deposited at the substrate temperatures of 25 °C, 400 °C, and 600 °C.

which was fabricated by the reactive-rf-magnetron sputtering technique and using a pure vanadium metal target under the mixed argon and oxygen gas atmosphere. However, the XRD patterns of sample SP25 revealed several varieties of vanadium oxide, which include V_2O_5, VO_2 (B), and V_6O_{13}. This result agrees with vanadium oxide thin films fabricated by ns-PLD and using the vanadium target under a mixture of argon and 10% oxygen gas atmosphere (D). These diffraction patterns match with the ICCD card numbers: 00-052-0794, 01-083-8516, and 04-007-1362. The Debye–Scherrer formula, $d = 0.9\lambda/\beta\cos\theta$ (where λ is the wavelength, β is the full width half maximum of the peak, 2θ is the scattering angle in radians) was used to estimate an average nanoparticle or grain size. The average grain size of these samples SP400 and SP600 is calculated to be 14 nm and 21 nm, respectively, for the diffraction peak centered at $2\theta = 27.90°$.

The surface morphology and cross section of the films were studied to understand the influence of the substrate temperature on the formation of VO_2 thin films. A focused ion beam (FIB, FEI Helios G4 CX DualBeam) approach was employed to mill and release a thick TEM lamella for *in situ* SEM. The microstructures of the VO_2 thin films comprising a large collection of nanoparticles or grains deposited on the substrate are shown in Figs. 4(a) and 4(b). The nanoparticles or grain sizes are spherical in shape and randomly distributed across the entire substrate surface of sample SP400 with an estimated average nanoparticle size of ∼12 nm (based on analysis using the ImageJ software). The average value of the nanoparticle radius obtained at the substrate temperature of 400 °C correlated well with that from the Debye–Scherrer formula calculation. In the case of sample SP600, the nanoparticles or grain sizes are non-uniformly distributed with irregular packing. The closed packed structure of sample SP600 is due to the higher temperature heating of the substrate that led to the agglomeration of the nanoparticles or the grains during deposition. Comparing the surface morphology of samples SP400 and SP600 with the sample fabricated at room temperature (shown in Fig. 1) clearly demonstrates that the substrate temperature has a significant effect on the quality of films produced and, on the nanoparticles, or grain sizes. A SEM cross-sectional analysis is performed to better understand the effect of the substrate temperature on the film growth under the stated deposition parameters of fs-PLD used in this research. The cross-sectional lamellae of the films were prepared by precise FIB milling and their corresponding SEM images are shown in Figs. 4(c) and 4(d). These illustrate a clear distinction between the VO_2 thin film deposited at two different substrate temperatures in terms of their porosity and thickness. The film deposited at 400 °C is more porous and thicker (1.2 μm) compared to the film deposited at 600 °C, which is thinner (0.75 μm) and less porous.

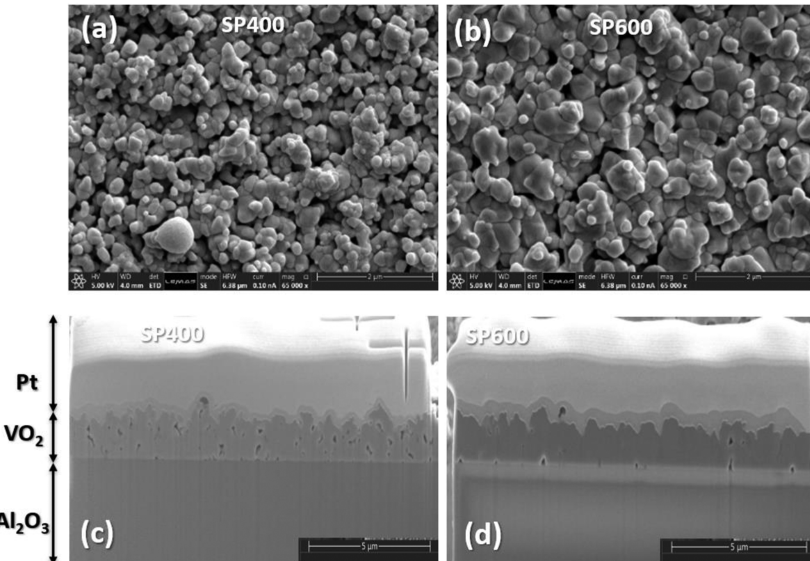

FIG. 4. SEM top-view microstructure image of the VO_2 thin film deposited onto the sapphire substrate at (a) 400 °C and (b) 600 °C. Cross-sectional interface between the VO_2 thin film and sapphire substrate at (c) 400 °C and (d) 600 °C.

© Author(s) 2020

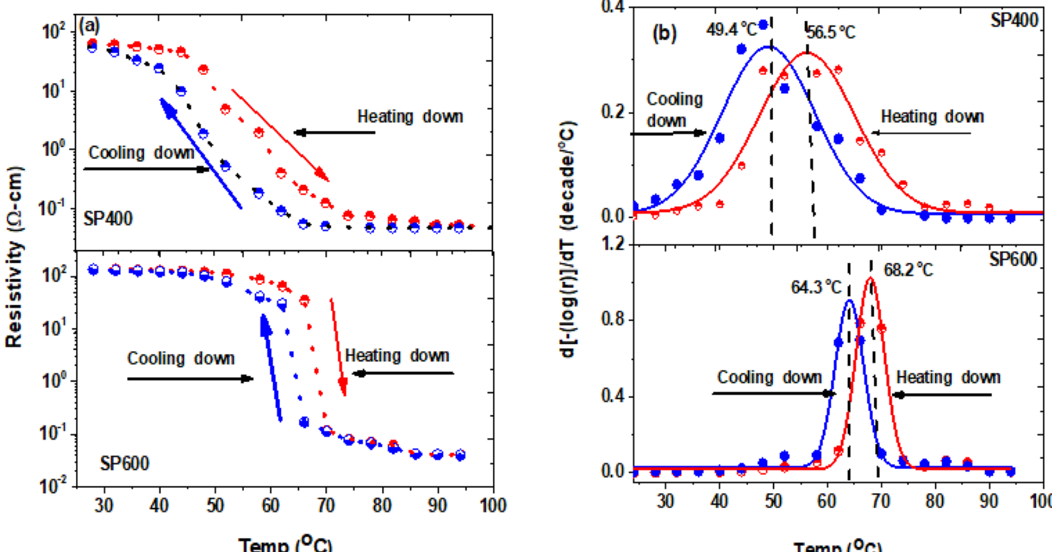

FIG. 5. (a) Electrical resistivity vs temperature behavior of VO_2 thin films grown on the sapphire substrate at different substrate temperatures: 400 °C (SP400) and 600 °C (SP600). (b) First derivative of $-\log_{10}(\rho)$ with respect to the temperature for heating (red, circle) and cooling (blue circle) curves.

B. Modulation of the VO_2 thin film phase transition temperature

In order to assess the characteristic MIT of grown VO_2 thin films and their suitability for applications we have carried out the measurement of their resistivity as a function of temperature. The electrical resistivity switching of the thin films was measured with a two-point probe made contacts technique at temperatures ranging from 20 °C to 100 °C in a step of 4.0 °C. Figure 5 illustrates the resistivity (ρ) as a function of the temperature for the heating and cooling cycles of the VO_2 thin films (SP400 and SP600). As shown in the figure, both VO_2 thin films undergo semiconductor MIT, when heated from room temperature to higher temperatures and vice versa. Sample SP600 exhibits a sharp and abrupt change in resistivity nearly four orders of magnitude in contrast to sample SP400 with three orders of magnitude change in resistivity switched. This indicates that sample SP600 is a better-quality thin film than sample SP400 in terms of electrical characteristics. The MIT parameters of the VO_2 thin films were determined by using the first derivative of the resistivity with respect to temperature {i.e., $d[-\log(\rho)]/dT$}.[56] A graph of $d[-\log(\rho)]/dT$ vs temperature was fitted to a Gaussian profile for the thermal cycle of heating (T_h) and cooling (T_c) [Fig. 5(b)], and then used to determine the four MIT parameters as well as the quality of the VO_2 films. The phase transition temperature is expressed as the average transition temperature between the T_h and T_c cycles, $\left(T_t = \frac{1}{2}(T_h + T_c)\right)$, while the thermal hysteresis width, (ΔH), is defined as the absolute temperature difference between T_h and T_c cycles transition, ($\Delta H = |[(T_h - T_c)]|$). The sharpness is characterized by the full width half maximum (FWHM) and the amplitude (ΔA in decades) is expressed as the $\log_{10}$ of the ratio of change in resistivity between metallic-to-insulating stages. The MIT characteristics of samples SP400 and SP600 are reported in Table I.

According to Gaussian fittings on the derivative logarithmic plots of resistivity, the MIT heating and cooling temperatures of the VO_2 thin film grown at a substrate temperature of 400 °C (SP400) are determined to be 49.4 °C and 56.5 °C, respectively, as shown in Fig. 5(b). This corresponds to an average MIT temperature of 53 ± 2.6 °C, while MIT temperatures of 64.3 °C and 68.2 °C are observed for heating and cooling of the sample SP600, respectively. An average transition temperature of ~66 ± 2.5 °C is obtained, which is closer to that of a bulk VO_2 material (68 °C).[8] Previous studies by Kana *et al.*[57] demonstrated that the MIT transition temperature depends on the VO_2 film thickness; thinner films have shown higher transition temperatures. Sample SP600 with a film thickness of 0.75 μm reveals a narrower hysteresis width temperature of ~3.9 °C as compared to 7.2 °C of sample SP400, which is 1.3 μm thick. It had also been demonstrated that the surface morphologies such as grain size distribution and boundary interface have profound consequence on the VO_2 thin film MIT characteristics,[58] especially, transition temperature and amplitude. Thus, the difference between these two samples' MIT parameters can be attributed to the increase in the substrate temperature, which leads to the increase in nanoparticles or grain sizes. Moreover, the increase in the substrate temperature enhances the nanoparticles' compactness and decreases the nanoparticle/grain boundaries, as given in Fig. 4. Hence,

TABLE I. The MIT characteristics of the as-deposited VO_2 (M1) thin films.

Sample ID	T_t (°C)	ΔH (°C)	FWHM (°C)	ΔA (decades)
SP400	53 ± 2.6	7.2 ± 0.2	21.0	3.1 ± 0.1
SP600	66 ± 2.5	3.9 ± 0.1	7.0	3.5 ± 0.1

© Author(s) 2020

sample SP600 exhibits the good quality of VO_2 (M1) thin film because the phase transition temperature of the heating process is around 68.2 °C, which matches with the transition temperature of a bulk VO_2 sample. In addition, sample SP600 has lower ΔH and higher ΔA values as depicted in Table I, while the T_t and ΔH values are analogous to many studies reported elsewhere.[30,32,35] For instance, Cheng *et al.*[59] synthesized the VO_2 thin film onto the 6H–SiC substrate by employing the VO_2 ceramic target and ns-PLD technique. Their results indicate that the phase transition temperatures range from 66 °C to 70 °C, which is consistent with our measurements. In contrast, sample SP400 is not of good-quality VO_2 thin film owing to its smaller nanoparticle or grain sizes, grain boundaries, high nucleation or porosity defects on the surface, and cross section. This can be explained by the low ΔA and high ΔH values with a broad and low phase transition temperature of about 53 ± 2.6 °C. Such low transition temperature and broad thermal hysteresis width characteristics could be attributed to the amorphous or randomized polycrystalline VO_2 thin film. The low transition temperature and amplitude as well as broad hysteresis width obtained in the thin film grown at 400 °C could be attributed to the fact that the film growth condition was far below the optimized condition required. Bhardwaj *et al.*[8] recently fabricated a VO_2 (M1) thin film on the silicon-on-silica substrate by reactive PLD with the vanadium target. A phase transition temperature of 55 °C was obtained at a substrate temperature of 600 °C under the oxygen pressure of 50 mTorr. Furthermore, the non-uniformity of the thin film surface and porosity could have been attributed to the low MIT temperature and high sharpness values. These results are comparable to Brassard *et al.*[55] where they grew the high-quality polycrystalline VO_2 (M1) thin films on the Si_3N_4/Si substrate by employing the reactive rf-magnetron-sputtered technique with the thickness range from 50 nm to 350 nm. They obtained a phase transition temperature of 69 ± 2 °C regardless of the film thickness, however, the MIT sharpness and hysteresis width decreased from 9 °C to 3 °C and 12 °C to 7.5 °C by increasing the film thickness. Hence, the thicker and good-quality polycrystalline VO_2 thin film could be ascribed to the excellent characteristics of the VO_2 film's semiconductor to metal transition.

IV. CONCLUSION

In conclusion, the fs-PLD technique has been successfully used for synthesizing high-quality VO_2 (M1) thin films on sapphire (0001) substrates with a V_2O_5 target at the substrate temperatures of 400 °C and 600 °C. The surface morphological analyses were carried out by SEM to evaluate the influence of the substrate temperature on the nanoparticles or grain size. It is observed that the nanoparticle or grain size increases with an increase in the substrate temperature to form agglomerated nanoparticles or grains, whilst the surface roughness of the films improves considerably. The structural characterization performed by Raman scattering and XRD measurements confirmed the presence of high-quality VO_2 (M1) phase films for both samples. The electrical resistivity switching of the VO_2 thin film MIT was thermally activated by three to four orders of magnitude change in the resistivity and MIT width of 3.9 °C for sample SP600. The structural and electrical characteristics of the VO_2 (M1) film fabricated by the fs-PLD technique could be attractive for thermochromic smart windows and tunable antenna applications.

ACKNOWLEDGMENTS

This research was funded by the Engineering and Physical Sciences Research Council through the SeaMatics research and Ultrafast Laser Plasma Implantation Grants (Grant Nos. EP/M015165/1 and EP/M022854/1). The author from Heriot-Watt University acknowledges in part support from EU H2020 Marie Skłodowska-Curie Individual Fellowship No. 840854, ViSionRF. We also thank Mr. John Harrington at the Leeds Electron Microscopy and Spectroscopy (LEMAS) Centre, for support in carrying out the SEM and FIB cross section measurements.

DATA AVAILABILITY

The data that support the findings of this research work are available from the corresponding author upon reasonable request.

REFERENCES

[1] A. D. Wadsley, Acta Crystallogr. **10**, 261 (1957).
[2] M. Nazari, Y. Zhao, Z. Y. Fan, K. Ziemer, A. A. Bernussi, and M. Holtz, J. Phys. D: Appl. Phys. **48**, 135101 (2015).
[3] F. J. Morin, Phys. Rev. Lett. **3**, 34 (1959).
[4] S. Kachi, K. Kosuge, and H. Okinaka, J. Solid State Chem. **6**(2), 258–270 (1973).
[5] U. Schwingenschögl and V. Eyert, Ann. Phys. **13**, 475 (2004).
[6] C. Leroux and G. Nihoul, Phys. Rev. B **57**(9), 5111–5121 (1998).
[7] S. Lee, I. N. Ivanov, J. K. Keum, and H. N. Lee, Sci. Rep. **6**, 19621 (2016).
[8] D. Bhardwaj, A. Goswami, and A. Umarji, J. Appl. Phys. **124**, 135301 (2018).
[9] G. Seo, C. Ko, B.-J. Kim, and Y. Cui, IEEE Electron Device Lett. **32**(11), 1582–1584 (2011).
[10] G. Gopalakrishnan, D. Ruzmetov, and S. Ramanathan, J. Mater. Sci. **44**(19), 5345–5353 (2009).
[11] C. N. R. Rao, Annu. Rev. Phys. Chem. **40**, 291–326 (1989).
[12] J. Jeong, N. Aetukuri, T. Graf, T. D. Schladt, M. G. Samant, and S. S. P. Parkin, Science **339**, 1402–1405 (2013).
[13] Z. Yang, C. Ko, and S. Ramanathan, Annu. Rev. Mater. Res. **41**, 337–367 (2011).
[14] Y. Tokura, Phys. Today **56**(7), 50–55 (2003).
[15] M. Soltani, M. Chaker, E. Haddad, R. V. Kruzelecky, and J. Margot, Appl. Phys. Lett. **85**, 1958–1960 (2004).
[16] M. Rini, Z. Hao, R. W. Schoenlein, C. Giannetti, F. Parmigiani, S. Fourmaux, J. C. Kieffer, A. Fujimori, M. Onoda, S. Wall, and A. Cavalleri, Appl. Phys. Lett. **92**, 181904 (2008).
[17] J. Zhou, Y. Gao, Z. Zhang, H. Luo, C. Cao, Z. Chen, L. Dai, and X. Liu, Sci. Rep. **3**, 3029 (2013).
[18] F. Dumas-Bouchiat, C. Champeaux, A. Catherinot, and A. Crunteanu, Appl. Phys. Lett. **91**(22), 223505-1–223505-3 (2007).
[19] H. Liu, J. Lu, and X. R. Wang, Nanotechnology **29**, 024002 (2018).
[20] L. Huitema, A. Crunteanu, H. Wong, and E. Arnaud, Appl. Phys. Lett. **110**, 203501 (2017).
[21] H. Kim, K. Cheung, R. C. Y. Auyeung, D. E. Wilson, K. M. Charipar, A. Piqué, and N. A. Charipar, Sci. Rep. **9**, 11329 (2019).
[22] C. Hillman, P. Stupar, J. Hacker, Z. Griffith, M. Field, and M. Rodwell, in *IEEE International Microwave Symposium Digest* (IEEE, 2014), pp. 1–4.
[23] J. Givernaud, A. Crunteanu, J.-C. Orlianges, A. Pothier, C. Champeaux, A. Catherinot, and P. Blondy, IEEE Trans. Microwave Theory Tech. **58**(9), 2352–2361 (2010).
[24] T. S. Teeslink, D. Torres, J. L. Ebel, N. Sepulveda, and D. E. Anagnostou, IEEE Antennas Wireless Propag. Lett. **14**, 1381–1384 (2015).

© Author(s) 2020

[25]D. E. Anagnostou, D. Torres, T. Teeslink, and N. Sepulveda, IEEE Antennas Propag. Mag. **62**, 58 (2020).
[26]N. Wang, S. Liu, X. T. Zeng, S. Magdassi, and Y. Long, J. Mater. Chem. C **3**, 6771–6777 (2015).
[27]S. Zhang, I. S. Kim, and L. J. Lauhon, Nano Lett. **11**, 1443–1447 (2011).
[28]A. Petraru, R. Soni, and H. Kohlstedt, Appl. Phys. Lett. **105**, 092902 (2014).
[29]J. Jian, A. Chen, W. Zhang, and H. Wang, J. Appl. Phys. **114**, 244301 (2013).
[30]N. A. Charipar, H. Kim, E. Breckenfeld, K. M. Charipar, S. A. Mathews, and A. Pique, Appl. Phys. A **122**(1-5), 512 (2016).
[31]S. Chen, J. Lai, J. Dai, H. Ma, H. Wang, and X. Yi, Opt. Express **17**(26), 24153 (2009).
[32]N. Shukla, A. Parihar, E. Freeman, H. Paik, G. Stone, V. Narayanan, H. Wen, Z. Cai, V. Gopalan, and R. Engel-Herbert, Sci. Rep. **4**, 4964 (2014).
[33]G. Rampelberg, M. Schaekers, K. Martens, Q. Xie, D. Deduytsche, B. De Schutter, N. Blasco, J. Kittl, and C. Detavernier, Appl. Phys. Lett. **98**, 162902 (2011).
[34]P.-R. Zhu, S. Yamamoto, A. Miyashita, and H. Naramoto, Chin. Phys. Lett. **15**(12), 904 (2008).
[35]D. H. Kim and H. S. Kwok, Appl. Phys. Lett. **65**, 3188 (1994).
[36]O. A. Novodvorsky, L. S. Parshina, and O. D. Khramova, Bull. Russ. Acad. Sci.: Phys. **80**(4), 376–380 (2016).
[37]K. Shibuya and A. Sawa, AIP Adv. **5**, 107118 (2015).
[38]S. Majid, D. K. Shukla, F. Rahman, K. Gautam, V. G. Sathe, R. J. Choudhary, and D. M. Phase, J. Phys.: Conf. Ser. **755**, 012027 (2016).
[39]S. Beke, L. Kőrösi, S. Papp, L. Nánai, A. Oszkó, J. G. Kiss, and V. Safarov, Science **254**(5), 1363–1368 (2007).
[40]R. K. Singh, D. Bhattacharya, and J. Narayan, Appl. Phys. Lett. **57**, 2022 (1990).
[41]S. B. Wang, S. B. Zhou, G. Huang, and X. J. Yi, Surf. Coat. Technol. **191**, 330 (2005).
[42]J. H. Li, N. Y. Yuan, and J. S. Xie, Appl. Surf. Sci. **243**, 437 (2005).
[43]C. Chen, X. Yi, J. Zhang, and X. Zhao, Infrared Phys. Technol. **42**, 87 (2001).
[44]E. K. Barimah, M. W. Ziarko, N. Bamiedakis, I. H. White, R. V. Penty, and G. Jose, Opt. Mater. Express **8**(7), 1997–2007 (2018).
[45]J. Perrière, C. Boulmer-Leborgne, R. Benzerga, and S. Tricot, J. Phys. D: Appl. Phys. **40**, 7069–7076 (2007).
[46]G. Stefanovich, A. Pergament, and D. Stefanovich, J. Phys.: Condens. Matter **12**, 8837 (2000).
[47]H.-T. Kim, B.-G. Chae, D.-H. Youn, S.-L. Maeng, G. Kim, K.-Y. Kang, and Y.-S. Lim, New J. Phys. **6**, 52 (2004).
[48]H.-T. Kim, B.-J. Kim, S. Choi, B.-G. Chae, Y. W. Lee, T. Driscoll, M. M. Qazilbash, and D. N. Basov, J. Appl. Phys. **107**, 023702 (2010).
[49]W.-J. Shen, K. W. Sun, and C. S. Lee, J. Nanopart. Res. **13**, 4929–4936 (2011).
[50]S. T. Oyama, G. T. Went, K. B. Lewis, A. T. Bell, and G. A. Somorjai, J. Phys. Chem. **93**(18), 6786–6790 (1989).
[51]J. Z. Wang and K. E. Gonsalves, J. Comb. Chem. **1**, 216–222 (1999).
[52]P. Shvets, O. Dikaya, K. Maksimova, and A. Goikhman, J. Raman Spectro. **50**, 1226 (2019).
[53]F. Ureña-Begara, A. Crunteanu, and J.-P. Raskin, Appl. Surf. Sci. **403**, 717–727 (2017).
[54]K. R. Asmis and J. Sauer, Mass Spectrom. Rev. **26**, 542–562 (2007).
[55]D. Brassard, S. Fourmaux, M. Jean-Jacques, J. C. Kieffer, and M. A. El Khakani, Appl. Phys. Lett. **87**, 051910 (2005).
[56]A. Moatti, R. Sachan, J. Prater, and J. Naraya, ACS Appl. Mater. Interfaces **28**(9), 24298 (2017).
[57]J. B. K. Kana, J. M. Ndjaka, P. O. Ateba, B. D. Ngom, N. Manyala, O. Nemraoui, A. C. Beye, and M. Maaza, Appl. Surf. Sci. **254**(13), 3959–3963 (2008).
[58]H. Zhang, Z. Wu, C. Wang, and Y. Sun, Vacuum **170**, 108971 (2019).
[59]X. Cheng, Q. Gao, K. Li, Z. Liu, Q. Liu, Q. Liu, Y. Zhang, and B. Li, Nanomater **9**, 1061 (2019).

© Author(s) 2020